Elsevier Editorial System(tm) for Sensors & Actuators: B. Chemical

Manuscript Draft

Manuscript Number:

Title: Cost-effective fabrication of polycrystalline TiO2 with tunable n/p conductivity for selective hydrogen monitoring

Article Type: Research Paper

Keywords: gas sensors; TiO2; n/p conductivity inversion; power consumption; thermal oxidation

Corresponding Author: Dr. Azhar Ali Haidry, Ph.D.

Corresponding Author's Institution: College of Material Science and Technology

First Author: Azhar Ali Haidry, Ph.D.

Order of Authors: Azhar Ali Haidry, Ph.D.; Linchao Sun ; Bilge Saruhan; Andrej Plecenik; Tomas Plecenik; Honglie Shen; Zhengjun Yao

Abstract: In this report, we demonstrate a simple and cost-effective strategy to prepare polycrystalline rutile TiO2 based gas sensors with tunable n/p type conductivity inversion depending on gas concentration, operating temperature and applied voltage. The effect of surface modification by Ag and Ni thin film on structural, morphological and gas sensor characteristics is studied in detail. The sensors show excellent sensing performance in terms of sensitivity (~25% for 0.1 vol. % H2 diluted in technical air), selectivity (selectivity factor for 0.1 vol. % H2 is about ~24 against NH3, CH4, NO2 and ~8 for CO), stability (both long-term and short-term) and reaction times (~0.7 min for 0.1 vol. % H2). The aforementioned performance is recorded at 300 °C with applied voltage of 0.1 V. Excluding the power consumption of sensor heater (typically ~5□10-5 watt), this applied voltage 0.1 V can reduce the power consumption to 3□10-10 watt. We found a critical point, defined with threshold-concentration (CTh), threshold-temperature (TTh) and critical-voltage (VC), at which the conductivity inverses from one kind to another, something intriguing to novel sensing phenomena that can be exploited to tailor the selectivity of the sensors. A physical-chemical sensing model is presented to understand the aforesaid peculiar occurrence.

Suggested Reviewers: Sheikh Akbar PhD
Materials Science Engineering, Ohio State University
akbar.1@osu.edu
Dr. Sheikh A. Akbar is a Professor of Materials Science and Engineering and Founder of the National Science Foundation (NSF) Center for Industrial Sensors and Measurements (CISM) at The Ohio State University in Columbus, OH, USA.He is an expert on this topic of synthesis-microstructure-property relations of electronic ceramic bulk, thin-film and nano-structures.

Klaus Schierbaum PhD
Institute of Experimental Physics of condensed materials

schierb@uni-duesseldorf.de
Prof. Klaus Schierbaum is an Expert in the materials science based on Thin Films and Nanotechnology and Physical Chemistry.

Anton Köck PhD
Materials Center Leoben
anton.koeck@mcl.at
Professor Anton Koeck is a Key Researcher, majoring in related fields of gas sensor in Materials Center Leoben.

Ivan Hotovy PhD
Slovak Technical University
ivan.hotovy@stuba.sk
Ivan Hotovy is an expert on this topic of metal oxide thin films at Slovak University of Technology.

Xiaogan Li PhD
Dalian University of Technology
lixg@dlut.edu.cn
Professor Xiaogan Li is famous in following field of High performance semiconductor sensitive and energy materials, Nano sensitivity and energy materials Electronics and Sensors and new energy devices and detection systems.

ABSTRACT

In this report, we demonstrate a simple and cost-effective strategy to prepare polycrystalline rutile TiO_2 based gas sensors with tunable n/p type conductivity inversion depending on gas concentration, operating temperature and applied voltage. The effect of surface modification by Ag and Ni thin film on structural, morphological and gas sensor characteristics is studied in detail. The sensors show excellent sensing performance in terms of sensitivity (~25% for 0.1 vol. % H_2 diluted in technical air), selectivity (selectivity factor for 0.1 vol. % H_2 is about ~24 against NH_3, CH_4, NO_2 and ~8 for CO), stability (both long-term and short-term) and reaction times (~0.7 min for 0.1 vol. % H_2). The aforementioned performance is recorded at 300 °C with applied voltage of 0.1 V. Excluding the power consumption of sensor heater (typically ~5×10^{-5} watt), this applied voltage 0.1 V can reduce the power consumption to 3×10^{-10} watt. We found a critical point, defined with threshold-concentration (C_{Th}), threshold-temperature (T_{Th}) and critical-voltage (V_C), at which the conductivity inverses from one kind to another, something intriguing to novel sensing phenomena that can be exploited to tailor the selectivity of the sensors. A physical-chemical sensing model is presented to understand the aforesaid peculiar occurrence.

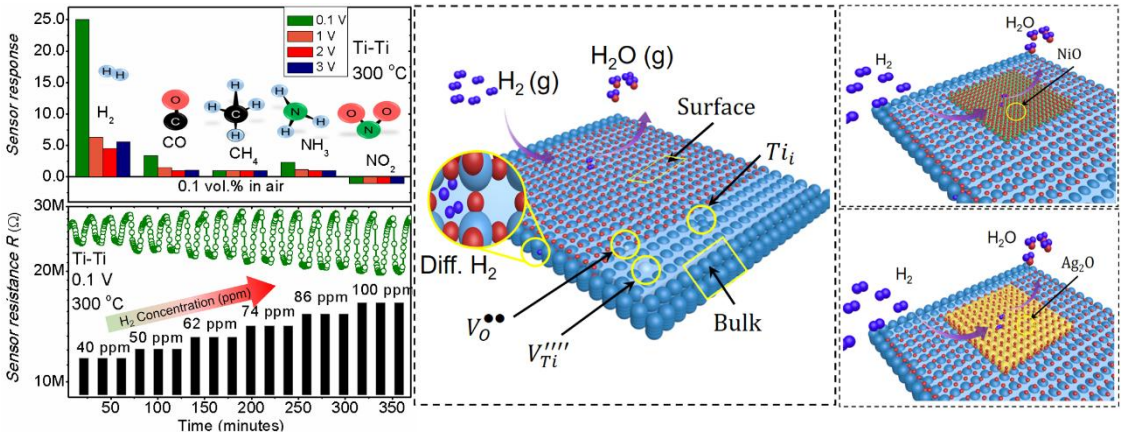

Cost-effective fabrication of polycrystalline TiO_2 with tunable n/p conductivity for selective hydrogen monitoring

Azhar Ali Haidry[a,*], Linchao Sun[a], Bilge Saruhan[b], Andrej Plecenik[c], Tomas Plecenik[c], Honglie Shen[a], Zhengjun Yao[a]

[a]College of Materials Science and Technology (MST), Nanjing University of Aeronautics and Astronautics (NUAA), JiangJun Avenue 29, Nanjing 21101, P. R. China
[b]Institute of materials research, German Aerospace Center (DLR), Linder Hoehe, 51147 Cologne, Germany
[c]Department of Experimental Physics, Faculty of Mathematics, Informatics and Physics, Comenius University Bratislava
*Corresponding authors Tel.: +8615895837907; Fax: +86-25-52112626.
E-mail addresses of corresponding author: aa.haidry@nuaa.edu.cn; azharalig2@gmail.com

1. Introduction

Unlike the previous decades, in the last few years, there is a rapid rising demand on low-cost, highly sensitive, and selective gas monitoring smart systems to be utilized in various modern industries. Chemical sensors based on nanostructured metal oxide semiconductors (MOX) offer great opportunity to meet this demand as a consequence of their superior sensing properties in detecting and monitoring of various toxic and explosive gases [1-3]. Concomitantly, besides the selectivity and operating temperature issues, the recent discovery of n-p-n type conductivity transition with gas exposure has triggered new matter to be addressed. Recently, many articles have reported on this transition behavior from n- to p-type conductivity or the opposite, for pure MOX, doped MOX and for its composites [4-11]. The explanation of conductivity transition is a matter of debate in recent times since the factors causing this phenomenon are manifold, such as temperature [4-7], gas concentration [4-9] composition [4, 10], and impurity concentration [11, 12]. However, there is no doubt that the conductivity transition is related to the surface charge effect, leading to the transformation of the type of dominant charge carriers [13-14].

Titanium dioxide or titania (TiO_2) belongs to the MOX group and exhibit not only excellent sensitivity, but stability even in harsh conditions and elevated temperatures [15-18]. It has already been experimentally proved that bulk TiO_2, in general, exhibits n-type conductivity with electrons being dominant surface charge carriers and having ionized donors at room temperature with the density of electrons $[e^-]$ equals the density of donors N_D ($[e^-] = N_D = 10^{17}–10^{20}$ cm^{-3}), small effective mass m^* (~ 0.1–0.4 m_e) and mobility in the range μ=1–50 cm^2/Vs. Depending on the circumstances, many factors can be considered to influence the charge carrier density ($[e^-]$~$10^{16}–10^{18}$ cm^{-3}) and the mobility value (μ~$10^2–10^3$ cm^2/Vs), including grain boundaries, ionized impurities and electron-phonon interactions. For example, the grain boundaries in polycrystalline TiO_2 contain very high densities of surface states that results in depleted grains and capture (or scatter) free charge carriers to generate a potential barrier (~eV_s). On the contrary, TiO_2 can also be classified as p-type semiconductor due to dominant counterpart surface charge carriers, the holes. For n-type TiO_2 based gas sensors, the resistance value decreases when the surface is exposed to reducing gases (e.g. H_2, CO) as conversely occurs for oxidizing gases (e.g. NO_2, O_2).

The authors have already published several reports on improved hydrogen gas sensing properties of TiO_2 coatings even at room temperature through the control of electrode

configuration [19-21]. However, there are only limited reports [10-11] in the literature on the conductivity transition behaviour of TiO_2. Nanostructured TiO_2 was facilely fabricated via simple thermal oxidation of Ti-discs. In addition, very thin (~ 30 nm) layer of Ni and Ag was sputtered on the top surface prior to thermal oxidation to achieve differences in morphology and conductivity. To authors' best knowledge, for the first time, in this report the factors that influence the conductivity change of rutile TiO_2 are explored. From a fundamental viewpoint, the dependence of the conductivity on the operational parameters can pose serious limitations to the practical exploitation of the proposed sensor. In addition, the work provides a conceptual advance in the field of semiconductor metal oxide gas sensors, where we demonstrate the inherent n/p type electrical conductivity inversion of TiO_2 with gas exposure by engineering the surface charge carriers. The proposed strategy in this report can make significant impact on the development of future smart gas sensors and should be applicable to other materials in this area.

2. Experimental

2.1 Fabrication of gas sensors

As a raw material, high purity Ti-discs (99.9% purity) having diameter of ∅=15 mm and thickness of 1 mm was purchased from BaoTi Group Co. Ltd. At first, the discs were washed using ultrasonic bath in sequence in acetone, ethanol, and deionized (DI) water for each 15 min, respectively, to remove oil and subsequently dried at 90 °C for 5 min. Thereafter, both sides of Ti-discs were polished for 20 min using the abrasive metallographic paper from type 0# (W40) to 05# (W7) until the surface become highly smooth. After continuous polishing for 10 min on the polishing machine, the Ti-discs were repeatedly washed again using ultrasonic oscillation for 10 min in acetone, ethanol and DI water bath, respectively, in order to remove any available surface impurities. Afterwards, thin films ~ 30 nm of Ti, Ni, and Ag were deposited on the dried Ti-discs using RF magnetron sputtering (MSIB-6000 magnetron sputtering/ion beam sputtering machine from Beijing Chuangweina Tech. Co. Ltd) by means of controlling power and time accurately. Finally, nanostructured TiO_2 films modified with Ti, Ni, and Ag oxides were obtained via thermal oxidation under static air condition. During oxidation process the samples were placed in porcelain combustion boats in tube furnace OTF-1200X tubular furnace (Hefei Kejing Materials Technology Co. Ltd) and the temperature was increased to 1000 °C with heating rate of 10 °C/min. The furnace temperature under the mentioned conditions was kept at 1000 °C for 1 h and subsequently cooled down naturally to room temperature with a slow rate.

The interdigitated electrodes with a spacing of 10 μm were fabricated by photolithography method. To start with, the lift-off photoresist (35E and AZ 5214E) was deposited by spin coating on the surface of oxidized TiO_2, followed by the exposure to 200 W Hg discharge lamp through a mask with comb-like structures. Then platinum layer of 20 nm thickness was deposited by DC magnetron sputtering process. In a typical DC magnetron sputtering of platinum process, a voltage source Swinstek GPR – 60H15D (Cathode voltage – Uk = 380 V with current limit I = 80 mA) was used, the distance between target and substrate was kept at 4 cm, the base pressure was ~10^{-3} Pa. The sputtering process was conducted in a closed vacuum chamber in continuous argon flow mode at working pressure of 0.5 Pa. The growth rate of Pt layer with these parameters was ~0.5 nm/s. Eventually, the samples were put in

acetone to remove photoresist. The detailed thermal oxidation process and the sensor fabrication technique have been reported in our previous studies elsewhere [22-24]. The schematic diagram of overall preparation steps is shown in Fig. 1.

2.2 Characterization

The crystal structure of the sensing films was confirmed by using Ultima IV X-ray diffraction (XRD) instrument from Japan with Cu Kα radiation (λ = 0.15406 nm) in the angle range of 10–80° at a scanning rate 5° min^{-1}. The MDI JADE 5.0 software was used for XRD pattern processing and determination of crystal phases in each sample by comparing the obtained peaks with reference Joint Committee on Powder Diffraction Standards (JCPDS) cards. The surface morphology was observed by Hitachi S-4700 scanning electron microscopy (SEM) from Japan. The sensing films structural details were further characterized by JEM-2100F transmission electron microscope (TEM, JEOL Ltd. Japan) operating at an accelerating voltage of 200 kV, equipped with Bruker energy dispersive spectrometer (EDS, from Germany).

The hydrogen sensing measurements were carried out using a self-established gas sensing measurement unit (Functional Materials and Chemical Sensor Lab, FuMS). With the aid of precisely controlled gas flow by mass flow controllers (MFC) from Vögtlin Instruments GmbH (GSC-A5SA-BB22), the gases flow to the pre-mixing cylindrical chamber of volume ~200 cm^3 simultaneously. The hydrogen concentrations were varied in the range of 40–1000 ppm by means of adjusting the flow ratio of 1000 ppm hydrogen (background technical air) and technical air. After passing 3 meters long gas pipeline with a diameter of ∅=6 mm, the mixing gases reaches the reaction chamber of volume ~350 cm^3 in the OTF-1200X tubular furnace (Hefei Kejing Materials Technology Co. Ltd), which determines the operating temperature of gas sensors. The model 6482 Dual-Channel Picoammeter/Voltage Source (Keithley, Tektronix US) was applied to measure the dynamic changes in the resistance/current of the sensor. The measurement unit enables to perform gas sensing measurement under different operating temperatures (up to ~1200 °C), applied voltages (±30 V) and atmosphere conditions. All the included instruments and experiment processes were accurately controlled by the independent research and development of in-house software based on LabVIEW program (Fig. S1 in ESI). The sensor response $SR=R_0/R_{H2}$ (R_0 is the stabilized resistance in dry technical air and R_{H2} is the saturated resistance in specific hydrogen concentration), and response (recovery) time, defined as and 90% change in the stable baseline (saturated gas) resistance, were estimated for the response analysis.

3. Results and Discussion

3.1 Phase and Crystal Structure

Notwithstanding the commercially available metallic titanium (Ti) discs and/or sheets are mainly characterized by the hexagonal closed packed alpha titanium (α-Ti) and body centered cubic beta titanium (β-Ti) phase, the oxides of titanium (e.g. TiO_2) are stamped as tetragonal anatase (A) and rutile (R), and orthorhombic brookite (B) phase. The XRD analyses, shown in Fig. 2, were performed to determine the constituent phases in each sample. As indicated by black filled circles in Fig. 2a, all the peaks at the XRD diffractogram

of as received (un-oxidized) Ti-disc (orange curve labelled as T0) were identified by comparing with standard powder diffraction card JCPD-44-1294, which shows the dominance of α-Ti phase with no other peak from β-Ti (JCPDS 44-1288) phase. The XRD diffractogram of the sample oxidized at relatively low temperature 600 °C (blue curve labelled as T6) still shows the dominant presence of α-Ti phase due to the exceeding penetration of X-rays through un-oxidized bulk of the disc. Very weak peak of rutile R (110) phase is appeared, which indicates very small fraction of initial rutile crystal phase formation in the mostly α-Ti phase disc. Upon oxidation, most probably due to the rise of surface titanium oxides the lattice parameters also increase yielding slight shift of α-Ti peaks to the right. The splitting of peaks at 38.45° and 70.69° is due to the formation of other titanium oxide (such as TiO_x) phases on the surface.

It appears that the degree of rutile crystallinity increases with oxidizing temperature as the intensity of α-Ti phase decreases. At higher oxidation temperatures 1000 °C (black curve labelled as T10), the α-Ti phase nearly disappears and transforms to rutile phase. However, the rutile phase is anisotropic (polycrystalline tetragonal) in nature, with *P*42/*mnm* space group and lattice constants a=b=4.593 Å and c = 2.959 Å, as its strong diffraction peaks at 2θ [°] = 27.44, 36.11, 54.39 and 56.71 are indexed to rutile TiO_2 phases (110), (101), (211) and (220) (JCPDS file No. 21-1276). There are low intensity peaks at 41.36° (111) and 44.19° (210), while the strongest one is (110) followed by (211).

The Fig. 2b demonstrates the XRD diffractograms of oxidized (at 1000 °C) TiO_2 modified with 30 nm Ti (black curve labelled as TO), Ni (red curve labelled as TNi) and Ag (olive green curve labelled as TAg) layers. The results exhibit peak intensity reduction and shift (towards right) of each rutile crystal; see the inset of R (110) peak in each curve of Fig. 2b. The peak intensity of R (110) crystal for un-modified TiO_2 is higher followed by TiO_2 modified with Ni and Ag respectively. On the other hand, the right shift of the peaks increases with Ni and Ag modifications. A slight increase in the peak intensity of TNi was found for R (211). After careful consideration of instrumental broadening, the grain size D_g of the rutile crystal for each sample was calculated by using standard Scherer formula $D_g = 0.9\lambda/B\cos\theta$, where λ = 0.15406 nm, B is described by the width of relevant diffraction peak profile at maximum height FWHM (in radians) and θ is the Bragg angle (in radians). For the most intense peak R (110), the grain size of TO was nearly same as that of TNi ~ 60 nm, while for TAg the grain size was small D_g = ~49 nm. In addition, for the samples TO, TNi and TAg, the grain size decreases for other rutile R (101)/(211) crystals, i.e. D_g = ~78/55, ~57/48 and ~53/39 nm.

To sum up, the un-annealed Ti-discs were metallic with only α-Ti phase. Under oxidizing conditions (in the present case static air) and high temperature treatment (in the present case at 1000 °C) the Ti-discs oxidize completely to TiO_2. The oxidized TiO_2 discs (TO, TNi and TAg) are polycrystalline in nature with a grain size in the range of ~ 39–78 nm. From the above analysis, it is inferred that the oxidized discs contains randomly oriented nano-grains of polycrystalline film. These findings, the reduced peak intensity as well as right shift, indicate the successful surface modification with oxides of Ni and Ag (i.e. NiO and Ag_2O). Due to anisotropic (polycrystalline) nature of the oxidized discs it is reasonable to assume that the peak shift (or mismatch 2θ values from reference database PDF cards) and intensity reduction are mainly caused by strain produced by defects in rutile crystals due to surface modification by Ti, Ni, and Ag thin coating and thus serve only for qualitative comparison

[25]. Moreover, it is remarkable to note that the α-Ti phase transforms into rutile phase without even going through anatase phase, the reason for which is unknown to the authors.

3.2 Microstructure and compositional analyses

On contrary, from the SEM micrographs in Fig. 3, it is evident that relatively large polycrystalline TiO_2 crystals in the submicron size ranging from ~0.2 to 2 μm are formed randomly after oxidizing Ti-dics at 1000 °C in oxygen rich environment (i.e. static air). The contrasting values of TiO_2 grains from XRD means the volume where the crystalline structure is intact and hence shows size of coherent domain. This happens when the grains contain defects such as dislocations. Thus one would say that the values obtained from SEM/TEM micrographs are more authentic. The surface of TiO_2@TiO_2 exhibits a periodically repeating (connected through their grain boundaries) submicron grains chain having an average size of ~600 nm, Fig. 3a. The surface of these well-organized submicron grains contains several TiO_2 nano-crystals (average size well below 100 nm) which grew courtesy of oxidized ~30 nm thin Ti coating, see the inset Fig. 3a-bottom. In addition, the EDX analysis and elemental mapping show a TiO_2 elemental composition near to stoichiometric order.

In comparison with TiO_2@TiO_2 surface, the TiO_2@NiO grains in Fig. 3b show extensive transformation in morphology and form steps-like terraces which grow along prismatic TiO_2 (100) rutile ledges. Albeit no NiO peaks were observed from above XRD analysis, the authors believe that such transformation is caused by ~30 nm Ni coating on Ti-disc surface. Interestingly to note that the effective ionic radius of Ag^+ (r_{ion}~1.21 Å) is twice of that Ti^{4+} (r_{ion}~0.60 Å), so the substitution of Ti^{4+} by Ag^+ is improbable as it would result in the expansion of TiO_2 lattice constants due to large ionic radii difference, which is not attested by our XRD data. On the other hand, the ionic radii of Ni^{2+} (r_{ion} ~0.69 Å) does not differ strikingly, so Ni^{2+} incorporation into TiO_2 lattice is highly possible, as lattice constants slightly changed for this case. In addition, due to the above mentioned fact, Ni modifies the surface significantly to give prominent step-like structure. By averaging the heights and widths of ten steps, the cumulative steps height and width is found to be ~10 and ~160 nm respectively. The values of steps heights (~10 nm) differ from the previously reported mono-steps heights values (~ 0.23 nm) [26], while the values of heights do not vary significantly. The reason for such differences may be related to the selection of single crystal TiO_2 wafer, wet chemical treatment and high-temperature oxidation under continuous oxygen flow [27]. Apparently no oxide nano-particles (either TiO_2 or NiO) on the surface was observed; however, the EDS mapping in the Fig. 3b-bottom shows the presence of Ni element (~0.86 at. %).

There appears to be only a few places on TiO_2@AgO surfaces where such steps-like terraces are formed. This suggests that the bulk-terminated rutile TiO_2 surface consists of polycrystalline submicron grains as shown in Fig. 3c. The micro-facets are also cleaved by occasional appearance of submicron rod like structures between the adjacent grains. The surface of the micro-facets also contain nanoparticles, to authors these refer to the oxides of silver yields during oxidation of ~30 nm Ag coating on Ti-disc, as suggested by the elemental mapping by EDS analysis, which confirms the presence of 0.95 at. % Ag, see Fig. 3c-bottom. The SEM results are in agreement with XRD results, and are further discussed and confirmed via TEM analysis below.

As observed in TEM images Fig. 4a-c, the average size of TiO_2@TiO_2 (~ 600 nm) is observed to be smaller than TiO_2@NiO (~2 μm), and TiO_2@AgO (~1.8 μm). Since, Ni^{2+} may replace Ti^{4+}, so its oxides were not fully seen in TEM micrographs, on the other hand, the traces of Ag_2O deposited on TiO_2 are already evident from TEM micrographs shown in Fig. S2 (ESI) as due to difference in contrast the black granular spots are superimposed in the background of large TiO_2 grains. In all samples, the bulk of the TiO_2 grains is characterized by R (110), R (101) and R (210) planes that correspond to d-values d [Å] ~3.25, 2.45 and 2.05 A respectively, see middle Fig 4a-c. Despite being highly stable, R (110) phase can undergo reconstruction depending on the degree of oxidizing temperature and environment [28]. In current case, nevertheless, the authors found the side faces of the rutile grains are mainly R (200) and R (111) corresponding to the d-values d [Å] ~2.28 and 2.19 respectively, see middle Fig 4a-c. The XRD peak intensity of R (111) of TiO_2@NiO has become sharper than that of un-modified sample, which suggests that the lattice fringes parallel to the side surface should be assigned to R (111) planes. Since these phases are not stable at higher temperature, so it is reasonable to assume hereinafter that the step-like structure appears on these faces. Despite that, as expected the selected area electron diffraction (SAED) pattern of TiO_2@TiO_2 sample shows relatively similar size rutile facets surface distribution. The SAED patterns of TiO_2@NiO and TiO_2@AgO indicate the formation some occasional large rutile crystal embedded in overall polycrystalline material, Fig. 4a-c on the right. The SAED pattern of TiO_2@TiO_2 is characterized by rings with occasional bright spots, where rings for TiO_2@NiO and TiO_2@AgO disappear nearly completely. This matches perfectly with SEM morphology where for TiO_2@AgO some rods of submicron dimension appeared on the surface (Fig. 3c). However, by measuring the d-values from SAED patterns, the rutile crystals indexed from the above XRD analysis were confirmed.

3.3 Electrical measurements and gas sensor tests

Based on surface adsorption, charge transfer and subsequent desorption of gas species, the sensing mechanism of TiO_2-based gas sensors as well as other MOX, such as SnO_2, ZnO, and In_2O_3 and so on is well established. Sensing at nano-scale is still challenging, since the control of critical defects play a great role. Moreover, the factors related to measurement conditions, such as operating temperature, applied voltage and specific gas concentration range, to conduct gas sensor tests can definitely affect the performance of the final device in real life applications. Most of the scientific papers, now-a-days, focus only on the laboratory based performance of these gas sensors. The factors that may lead to the false readings of the gas sensors are seldom reported. Towards this end, the authors found that the significant role of these factors is not only influence the final performance of a gas sensor, but also the inversion of the conductivity (n/p) type.

Sensor performance: After mounting the samples and prior to exploring the gas sensing characteristics, we kept the measuring chamber heated at particular operating temperature (200 – 400 °C) for at least 1 hour to achieve the chemical equilibrium on the sensor surface. Depending on the operating temperature, during this essential warm-up period the oxygen species (O_2^-, O^-, and O^{2-}) from air may be adsorbed on the sensor surface and subsequently diffused at the grain boundaries. To begin with, we firstly consider the performance of our sensor. We performed the gas sensor tests in operating temperature range of 200–400 °C with variable applied voltage range of 0.05–5 V for various reducing (H_2, CO, NH_3, and CH_4) and

oxidizing (NO_2) gases of 0.1 vol. % diluted in air. The sensors demonstrate high selectivity to H_2 gas in the presence of all these gases at all applied voltages under the same given experimental conditions and gas concentrations (Fig 5a). The value of selectivity factor (S_F), estimated as the response ratio of H_2 against other gases (1000 ppm), is circa constant S_F ~24 ($S_F = S_{R,H2}$) at 0.1 V against all gases except for CO where S_F drops to ~8. Meanwhile, the values of S_F drops significantly with increasing applied voltage (for instant at 1,2 and 3 V the respective values of S_F are ~7, 4 and 6) having the same ratio $S_F = S_{R,H2}$. The dynamic response of the sensors to above mentioned gases are shown in supplementary data (Fig. S3 in ESI). Despite our sensors show reproducible responses at all above mentioned parameters, it is found that the best operating temperature and applied voltage are 300 °C and 0.1 volt respectively. In combination with thermal activation energy, the influence of operating temperature and applied voltage will be discussed later in this section.

The typical sequential dynamic responses of Ti-Ti sensors measured at 300 °C with 0.1 V for the H_2 gas concentrations ranging from 40 to 100 ppm are shown in Fig. 5b. While the responses at 200 and 300 °C with 2 V are shown in Fig. S4 of ESI. As noticeable, at 0.1 V the Ti-Ti sensors show n-type semiconducting behaviour (i.e. decrease of resistance with reducing H_2 gas) with stable baseline resistance and fully reversible responses (e.g., S_R~1.5) for each concentration (e.g., 40 ppm). In comparison to Ti-Ti samples, the responses of Ti-Ag and Ti-Ni samples for high H_2 concentrations reduced, however; for low concentrations (e.g., 40 ppm) the responses improved (e.g., S_R~1.9 and S_R~4.8 for Ti-Ag and Ti-Ni respectively) with 0.1 V (see Fig. S5 in ESI). For further evaluation we plotted the sensor responses (R_0/R_g) against each corresponding H_2 concentrations in the inset of Fig. 5b. For low concentrations (below 100 ppm) the sensor response increases almost linearly with the H_2 concentration instead of following the power law dependency: that is $R_0/R_g \sim K_{H_2} C_{H_2}^m$, where "$K_{H2}$" is a response constant to H_2 and "m" is a coefficient of power law [35]. At other temperatures (200 □C and/or 400 □C) the sensor response is rather low, so it tends to saturate at certain increasing H_2 concentrations (e.g., 300 ppm), see Fig. S6 of ESI. And the comparison of the current work with previous works was shown in Table 1.

The short-term (i.e. repeatability) and long-term (i.e. reproducibility) stability of the sensors were checked to determine the surface poisoning effect that may lead to drift in the sensor signal and false measurements. The sensors suffering from surface poisoning need frequent calibration and are highly unsuitable for practical application. The short-term stability was confirmed by recording the repeating gas sensing measurements for a specific gas at least three times under the same experimental conditions (Fig. 5c). On the other hand, the long term stability was confirmed by the sensor tests performed with the specific time interval during which the sensors were kept in open air environment. The long-term stability tests are shown in Fig. 5d. The time interval between successive measurements in the figure is 1, 2, 14 and 120 day(s) respectively. As depicted in Fig. 5c, the sensor response after several months maintained the same reading level to all respective gas concentrations. For the application point of view, the performance of such sensor is extremely suitable where the sensor device can be placed near the muffler of the exhaust engine to monitor the hydrogen leakage.

In addition, it is highly important to estimate the response (τ_{Res}) and recovery (τ_{Rec}) times of a specific gas sensor. Here, the values of τ_{Res} and τ_{Rec} are specified as the necessary time to reach 90% of the saturated resistance value in the gas and 90% of the recovery to the initial baseline resistance value, respectively. The estimated values of τ_{Res} and τ_{Rec} as a function of

hydrogen concentration C_{H2} (ppm) in Fig. 5d indicate asymmetrical behaviour. This means, the values of τ_{Res}becomes shorter as H_2 concentration, C_{H2} increases, in turn, the values of τ_{Rec} becomes longer. For instance, for Ti-Ti sample at 200 °C under 2 V biasing, the values of τ_{Res} (τ_{Rec}) decrease (increase) from 2.2 to 0.7 (0.8 to 3.4) towards respective increasing hydrogen gas concentrations C_{H2} ~ 40 – 1000 ppm, respectively. Here relatively high estimated values of τ_{Res} and τ_{Res} are found than those mentioned in some previous reports [36]. The longer reaction times in our experiments can be explained on the basis of delay caused by gas evolution in gas mixing chamber and its further transportation through ~3 m long piping with an inner diameter of ∅~6 mm before it reaches to sensor surface. If an ideal gas mixing process is considered where C(t) represents the dynamic time dependent gas concentration, C_{mix} as the gas mixture concentration flowing towards the chamber and τ_{mix} (~0.87 min) as the time constant given by ratio of the test chamber volume (~350 cm^3) to the flow rate (400 sccm), then the gas evolution in the measurement chamber can be defined by the following differential equation:

$$\frac{dC(t)}{dt} = -\frac{C(t)-C_{mix}}{\tau_{mix}} \quad (1)$$

By applying the above mentioned parameters to the equation 1, the solution is given by the equation below:

$$C(t) = C_{mix} - C_{mix}\, e^{-1/\tau_{mix}} \quad (2)$$

Equation 2 gives the time-evolution of the actual concentration in the chamber after the ON/OFF cycle of the gas, e.g., for 1000 ppm H_2 the gas evolution is $\sim 1000 - 1000 \times e{-}0.015$. To further elaborate the response vs. recovery time asymmetry, we simulated the typical gas evolution process by using equation 2 for long period (30 minutes) and short period (10 minutes) as shown with our measurements in Fig. 5e. As can be seen that the gas evolution process takes several minutes before reaching the sensor surface, hence yielding relatively long reaction times as explained in previous reports elsewhere [37]. However, to achieve short reaction times the volume of the gas mixing cylinder and piping system should be as small as possible. Hence, in our case, it is reasonable to infer that the shortest possible reaction time constants we are able to obtain are thus limited by the gas mixing process and the real reaction times may be shorter.

In this work the most interesting results were the strong dependence of conductivity inversion (n/p) behaviour on the measurement conditions, such as the gas concentration, operating temperature and applied voltage (Fig. S7, 8 in ESI). The gas concentration-dependent and (operating) temperature-dependent conductivity inversion are reported previously for intrinsic [38], doped semiconductor [39] and mixed oxide composite films [40]. However, according to author's best knowledge, the voltage-dependent conductivity transition has not been studied previously. Strikingly, for each sample and each measurement condition, there exists a critical point at which the conductivity inverses. This is something which is intriguing to tailoring the selectivity of the sensors yielding novel sensing characteristics phenomena to be exploited. For further analysis and discussion, it is essential to define this critical point as threshold-concentration (C_{th}), critical-temperature (T_{th}) and critical-voltage (V_c).

Under ordinary circumstances, TiO_2 shows n-type response to reducing gases [19, 20] and

oxidizing gases [21]. Irrespective to the operating temperature, all sensors showed as expected n-type response to overall range of H_2 concentrations (40–100 ppm) at the lowest applied voltage 0.1 V. An inversion of conductivity from n- to p-type was observed for temperature below 300 °C at higher H_2 concentrations (e.g. C_{th} [ppm] ~ 750 and 825 at 200 and 250 °C). The values of C_{th} further decreases for the samples of Ti-Ag_2O (C_{th} [ppm] ~ 625 at 200 °C) and Ti-NiO (C_{th} [ppm] ~ 250 at 200 °C) at these temperatures. Whereas, for applied voltage 1 V and above the conductivity inverses to p-type at lower H_2 concentrations (Fig. 6a-c). At low operating temperatures the sensors show p-type behaviour for relatively low concentrations (e.g., 50 ppm or below) that inverses (p- to n-type) at higher H_2 concentrations, e.g., C_{th} [ppm] ~ 50, 74, 125, and 500 at T_W [°C] = 200, 250, 300, 350 and 400 °C. At higher applied voltages, the values of C_{th} increase for Ti-Ag_2O and Ti-NiO samples with increasing temperatures. It is also found that an inversion in conductivity occurs for high temperatures, which is time-dependent (Fig. 6d-f). For instance, the resistance of TiO_2 having p-type conductivity initially increases sharply above baseline stable resistance with H_2 concentration, then consequently overshoots above the saturated resistance in gas. For a fixed concentration, in this case, the first step is p-type response transient which reverses to n-type with jagged saturate resistance in H_2 gas. When the H_2 gas is turned OFF, the resistance again initially overshoots (instead of resistance decrease), and finally recovers to baseline resistance. This time-dependent phenomenon is observed for high H_2 concentrations, at high voltages and temperatures above 350 °C. The time-dependent conductivity inversion depends heavily on surface charge carriers and becomes dominant with Ag_2O and NiO modifications (Fig. 3).

In fact the aforementioned critical points are all linked together as depicted in Fig. 7a-d. Irrespective to the electrical conductivity inversion, n- to p-type (red open circles) or p- to n-type (green open up-triangles), C_{th} in Fig. 7a,c increases proportionally with working temperature. In contrast a decrease in C_{th} against increasing voltage is observed. On the other hand, both critical voltage and critical temperature decreases linearly against each other Fig. 7b,c. Meanwhile the surface modification of TiO_2 with Ag_2O and NiO brings further steep increase of the C_{th} against working temperature, see Fig. 7d.

4. Discussion of sensing mechanism

Above presented data enable us to infer that a polycrystalline TiO_2 must inevitably inhere twofold electrical conductivity and its inversion is universal phenomenon related to the intrinsic nature of sensing layer surface at which a specific gas analyte can significantly switch the concentration of charge carriers. The statement must be true as our TiO_2 contains large crystallites, with diameter (50–70 nm as estimated via XRD analysis) considerably surpasses the Debye-length, where the bulk may still shows n-type conductivity, and contrary, due to the pre-adsorbed oxygen present on the surface exhibits p-type conductivity. Various reports to account for such phenomenon have been published [41]. Nevertheless, the conductivity inversion contains decisively confutable arguments and remains, to date, still debatable. Following, we propose and discuss the hydrogen sensing mechanism together with selectivity and electrical conductivity inversion on the basis electrode-sensing layer interface, grain boundary charge transport via finite barriers connected in series and the inversion layer emanating due to acceptor levels creation just above the valence band.

To begin with, and as stamped by our conductivity inversion specifically with Ag_2O and NiO surface sensitization, we proceed with the fact that the sensor response is solely the surface reaction phenomena rather than the bulk (of Ti-discs) which contribute to the electrical conductivity only. This scenario for high voltage seems to be most likely improbable. In addition, it is also observed that Ag_2O and NiO migrate several nm deep into TiO_2 oxidized layer. Another fact that must be considered beforehand is the polycrystalline nature of our samples giving rise to the origin of grain boundaries. In our model which is sketched in Fig. 8a, for simplicity, we assume that the Pt-TiO_2 plays only a negligible role for low applied voltages. In this case, the sensor response can be attributed mainly to the change in intergranular surface potential eV_s in the vicinity between successive grains.

During oxidation process at higher-temperatures, oxygen from the surrounding static-air enters into metallic Ti-dics yielding rutile TiO_2 as a consequence of several reactions and formation of donor-type doubly ionized oxygen vacancies ($V_O^{\bullet\bullet}$) and titanium ($V_{Ti}^{''''}$) vacancies, and acceptor-type titanium interstitials (Ti_i). Later, under critical warm-up heating conditions in the presence of surrounding air and at temperature above 200 °C, firstly the sensor surface adsorbs ionic oxygen (O^- and/or O^{2-}) which trap surface charge carriers (mostly surface conduction electrons). According to J. Nowotny et al. [10], both these situations are extremely critical because pre-adsorbed oxygen results in a variation (being most likely reduction) of electrons (e') or holes ($h^\bullet$) concentration depending on whether it reacts with vacancies like oxygen ($O_O \rightleftharpoons V_O^{\bullet\bullet} + 2e' + 1/2\, O_2 + 2h^\bullet$) and titanium ($O_2 \rightleftharpoons VTi''''+2OO+4h\bullet$) or in rare cases with surface Ti ($2O2+3e'+O2+4h\bullet$). Under these circumstances, an insulating space charge region (so-called depletion layer) at the grain surface is formed where donor are initially immobile. Now consider the experimental conditions below critical point in an air flow, when electric field is applied (in our case the field generated by applied voltage below 1 V), initially all donors in this region become ionized and their concentration outnumbers their counterparts. The charge carrier density at this stage is still small, but gives rise to the inceptive n-type electron conductivity (usually very low for high band-gap TiO_2) and its transport is impeded by Pt-TiO_2 interface and thermally activated intergranular barriers (eV_s) connected in series.

The experimental data presented in Fig. 9 explicitly validate above mentioned assumptions. The characteristics of the I-V curves are found to be strongly dependent on C_{th} and T_{th} and account for the sensing mechanism basis. As expected, the symmetrical nonlinear I-V characteristics are obtained in air environment that correspond to the rectifying behaviour at both Pt/TiO_2 interfaces (Fig. 9a). To ensure better qualitative analysis the scan rate is fixed very low for accurate I-V measurements, the typical I-V curves containing the reverse biased conditions (negative applied voltage) are shown in Fig. S9 of ESI. A variation in I-V curves can be seen, although not significant as the qualitative rectification feature is maintained. This difference portends the variation in pre-adsorbed oxygen on the surface these samples. The thermionic field emission conduction mechanism and diffusion theory is valid here as our polycrystalline TiO_2 contains low carrier density. For this case, the Schottky barrier (ϕ_{SB}) heights for each sample can be estimated by $\phi_{SB} = k_B T \ln\left({I_S}/{AA^* T^2}\right)$, here KB is Boltzmann constant, T is temperature, A is the effective electrode area, A* is the Richard's constant, and I_S is saturation current which can be obtained by extrapolating the exponential increase of the current to zero applied voltage [42]. The calculated values of ϕ_{SB} for the TiO_2-TiO_2, TiO_2-Ag_2O and NiO samples are ~0.38, 0.34 and 0.33 eV respectively. The

values are quite distinct from the theoretically estimated value. For a comparative Pt/TiO_2 system, the difference of Pt work function (Φ_{Pt} ~5.65 eV) and TiO_2 electron affinity of (χ_{TiO2} ~4.16) should result in a Schottky barrier height of 1.44 eV. The lower ϕ_{SB} values in our case are understandable as during contact formation between Pt-electrodes and Pt-wires the silver paste is used as bond and further annealed at 550 °C to make it dry. This temperature is enough to diffuse Pt into TiO_2 several nm thickness [19, 43]. Fig. 9b confirms the second assumption, the electrical conductivity of our samples show strong dependent to the temperature. From Arrhenius curves, plotted with R-T data, the values of extracted thermal activation energies (which we denote as effective barrier height between the grains) are eV_s [eV] ~ 1.28, 1.32 and 1.73 for the TiO_2-TiO_2, TiO_2-Ag_2O and NiO samples respectively. For the fair comparison, we used the high temperature slope of Arrhenius plot for TiO_2-NiO sample, as it indicates two distinct eVs values (0.89 eV and 1.73 eV). Theoretically, on the basis of Pt electrode spacing (10 μm) and grain size which is estimated as an average of all rutile crystallites size, obtained from XRD analysis for TiO_2-TiO_2 (D_g~65 nm), TiO_2-Ag_2O (D_g~50 nm), and TiO_2-NiO (D_g~55 nm), the values of eV_s for TiO_2-TiO_2 should be smaller followed by TiO_2-NiO and TiO_2-Ag_2O, as number of grains (N_g) between the electrodes should follow the following sequence: TiO_2-TiO_2 (N_g~145), TiO_2-NiO (N_g~180) and TiO_2-Ag_2O (N_g~200). Hence, it can be inferred that for the large grains the effective eV_s values estimated by Arrhenius plots does not explicitly represent the average barrier heights of the depleted grains connected in series. Thus, the hypothesis – small grains lead to large eV_s values – is no longer valid. Apparently, in controlled dry air flow, the samples exhibit the conventional low charge concentration-based intrinsic characteristics.

Upon exposure, H_2 gas diffuse onto respective rutile TiO_2 surface and subsequently reacts with the pre-adsorbed oxygen to release captured immobile charge carriers that eventually reduce Pt-TiO_2 interface as well as the width of depletion region and intergranular barriers. To some extent this is true for unmodified TiO_2 under operating conditions below critical point. On the other hand, the origin of innate p-type TiO_2 sensor response to H_2 above the C_{th} and T_{th} can be understood on the basis of electronic band gap theory. As sketched in Fig. 8, the presence of surface defects give birth to intrinsic and extrinsic surface states that introduce energy levels with the forbidden energy gap of TiO_2. At this stage if acceptor concentration surpasses donors the depletion region spontaneously splits up in two distinct regions of e^- (above Fermi level) and h^+ (below Fermi level) majority carriers as sketched in Fig. 8b. The latter strongly gives rise to p-type conductivity and, thus, is known as inversion layer. Following the increase of H_2 concentration and operating temperature above their respective threshold value, the H_2-TiO_2 surface reaction leads in excess of localized acceptor levels [10] to fully demolish the depletion layer where inversion layer overtakes the sensing mechanism and its thickness consequently extends to increase the resistance. The selectivity towards H_2 can be accomplished by the fact that molecules of the other reducing gases (CO, CH_4 and NH_3) are too large and thus cannot diffuse through the surface to the bulk. The authors, however, believe that the selectivity of these sensors can be efficiently tuned by proper adjustment of the measurement conditions, specifically operating temperature and applied voltage.

Under H_2 exposure with low concentrations the sensor did not show rectifying behavior as shown in Fig. 9c. The electronic current first increases for low voltages and then decreases followed by another increase for further high applied voltages. This behavior is strongly related to conductivity inversion with threshold limit of the concentration. On the other hand, for high H_2 concentration, the current increases linearly and then saturates after 4 V. There is

an obvious decrease (~0.05–0.2 eV) in the Schottky barrier height for higher concentration, however, this is small as compared with high intergranular barrier height (~0.5–0.9 eV) for 200 ppm H_2 as shown in Fig. 9d. This observation again confirms our above mentioned assumption. With regard to the role of TiO_2 surface modification with Ag_2O and NiO towards low H_2 concentrations, the high sensor response can be attributed to the formation of n-p heterojunction at the sensors surface. The statement seems to be true only for low voltages. Conversely, p-p heterojunction is expected for high applied voltages (~2 V). As mentioned in the section 3.2 above, due to large difference in the effective ionic radius of Ag^+ and Ti^{4+}, so the substitution of Ti^{4+} by Ag^+ is improbable. While Ni^{2+} incorporation into TiO_2 lattice is highly possible ionic radii of Ni^{2+}. Both Ag and Ni begin to oxidize on the surface by taking electrons and their interface regions is the most favorable to provide e^-/h^+ recombination as it contains high defects concentration related to e^- traps or donors [45]. The electrons must transfer from TiO_2 to the Ag_2O and NiO, as TiO_2 has higher electronic fermi level. Thus additional depletion zone originates at the heterojunction to hinder the charge carrier transport and, consequently, under H_2 exposure the h^+ charges become dominant to give p-type conductivity.

The conventional models, however, fail to explain anomalous n/p conductivity inversion against applied field. The reason for this is obvious. Because the electrical resistance must decrease for typical n-type TiO_2 even in air flow environment with the rise of applied voltage as the electronic current flows through the bulk of the oxidized Ti-disc where the concentration of free conduction electrons (n_{cb}) increases directly with generated electric field. Mathematically, as reported in [46], for inter-digitated electrodes with known separation distance (s), electrode width (w), and applied voltage V_0, the electric field density E(x,y) and surface charge distribution σ(x) can be estimated by using following equations:.

$$E(x,y) = -\nabla V(x,y)$$

$$\sigma(x) = -2\varepsilon\left(\frac{2V_0}{\pi}\right)\left(\frac{1}{\sqrt{(2x/s)^2-1}}\right)\left(2/s\right)$$

Where

$$V = \frac{4V_0}{\pi}\sum_{n=1}^{\infty}\frac{1}{2n-1}J_0\left(\frac{(2n-1)\pi s}{2(s+w)}\right)sin\left(\frac{(2n-1)\pi x}{2(s+w)}\right)\left(-\frac{(2n-1)\pi|y|}{2(s+w)}\right)$$

For low applied voltages (below 1 V) on the same film, more than 90% of the electric current flows at the heavily packed with the pre-adsorbed oxygen near surface. Thus, the conductivity as well as the sensing mechanism is predominantly governed by intergranular active thermal barriers. On the other hand, for high voltage, the calculations with the known parameters (V_0 = 2 V, s=w=10 μm, y=0) would give high accumulated potential (~1.2 V) at the edges of the electrodes and an excess potential drop. This is a situation that cannot be applied in our case because of the fact that the electrodes along its sides have uniform dimensions. Now, as confirmed by SEM cross-section (not shown), if we consider 100 micron thick TiO_2 film and for 2 V applied voltage, about 85% of the current might flow deep 25 μm through the bulk of TiO_2 loaded with free conduction electrons (n_{cb}).

In agreement with the mentioned arguments R_{air} decreased from 650 MΩ to 8 MΩ with

voltage from 0.1 to 1 V. On the contrary, R_{air} value is increased from 200 MΩ to 500 MΩ when the voltage is further increased from 1 to 2 V. This is something contradicting the theory. This anomalous behavior can partially be validated in terms of electric potential fluctuation model and electron trapping-releasing process. As argumented by Konenkamp et al. [47], the existence of potential gradient must occur in comparative systems due to the presence of localized charges resulted by various defects. Under the high injection potential and ideal electron behavior, the electrons move away from the electric field and diffuse linearly to the electrode stripe where the pre-adsorbed oxygen on electrode edges account for the electron trap resulting in charge accumulation [46]. The result is high potential and electric distribution at the electrode stripe edges. At the same time, bulk oxygen vacancies become positively charged ionic center and act as another electron trap at higher voltage. The simultaneous trapping/releasing of the electron might happen within a fraction of second, and thus, compensating influence is exerted. For such case, the potential fluctuations are highly probable leading to invalidity of local charge neutrality condition. As both the amplitude and screening length of potential fluctuations are strongly dependent on n_{cb}, due to which the height of the Pt/TiO_2 Schottky interface would rather increase. This situation is in agreement of our I-V data where an unforeseen increase of Schottky barrier height is observed (Fig. 8d). Such high Schottky barrier height reduces the sensor response significantly as observed in our high voltage response and is consistent with previous reports [20]. This is an appealing and important feature of current study that offers relationship between sensor characteristics and measurement conditions. The study would notably help for the careful fabrication of future smart sensors for remote gas monitoring with controlled critical voltage, threshold temperature and gas concentration.

While the electric potential fluctuations and electron trapping/releasing mechanism enable us to clarify some of the conflicts in previous studies and describe the applied voltage effect on n- to p-type conductivity inversion, based on some assumptions, yet it does not account for some of the above properties in details. The method seems to be justified as long as the grain size is sufficiently large but becomes complicated with for small grains and films with low thickness. For this case, a better understanding of these mechanisms with the help of dc Hall measurements may therefore be necessary, which will allow explanation of the nature of dominant charge carriers. Our current setup does not allow us to perform such measurements. In-situ XPS analysis may be worthy to determine the formation of various other titanium oxide phases (such as Ti_nO_{2n-1} Magneli phases) with gas exposure under high applied voltage. In addition, due to the involvement of photoresist, developer and etchants in the electrode fabrication process on the sensor surface, one may expect surface contamination and extra surface defects. The role of active top Pt-electrode cannot be overruled, as Pt acts as a catalyst, something to be taken care in the future. These analyses, despite answering several questions, however, would extend out of the scope of this paper. Nevertheless, additional related work for better understanding of such complexities is planned as future collaboration among the authors.

5. Conclusion

A simple gas sensor configuration was designed for the detection of hydrogen at intermediate temperatures 200-400 °C. Intensive XRD studies show no significant changes in structure, meanwhile, morphological and surface chemistry states of TiO_2 were strongly altered by Ag_2O and NiO surface modification as attested by SEM and TEM analysis. The

sensors performance is excellent as it shows significant response (1.5) to low ppm H_2 (40 ppm) at given operating temperature (300° C) even with low applied voltage (0.1 V). The breakthrough data was obtained which shows strong correlation of sensor response with gas concentration (C_{Th}), operating temperature (T_{Th}) and applied biased voltage (V_C). This suggests that co-existence of both n- and p-type conductivity and its inversion, at threshold gas concentration (C_{Th}), operating temperature (T_{Th}) and applied voltage (V_C), is universal phenomenon found in polycrystalline TiO_2 that must be extended to other semiconducting metal oxides such as SnO_2, ZnO and etc. Further the detailed study of sensing mechanism and conductivity inversion enable the novel physical-chemical model which shows that dominant part of sensing mechanism is related to the variations in inversion layer and intergranular surface potential. We believe that these results and analyses provide significant conceptual as well as technological advance to open novel means in gas sensor technology to trigger enhance and selective monitoring of specific gas analyte.

Acknowledgements

This project was financially supported by the Priority Academic Program Development of Jiangsu Higher Education Institutions (PAPD) and Natural Science Foundation of Jiangsu Province project (BK20170795). The work was also partially supported by the Ministry of Education of the Slovak Republic under contract no. VEGA 1/0276/15. The authors also thank NUAA for providing start-up funding project.

References

Reference:

[1] A.C. Romain, J. Nicolas, Long term stability of metal oxide-based gas sensors fore-nose environmental applications: An overview, Sens. Actuators B 146 (2010) 502-506, https://doi.org/10.1016/j.snb.2009.12.027.

[2] K.J. Yoon, S.I. Lee, H. An, J. Kim, J.W. Son, J.H. Lee, H.J. Je, H.W. Lee, B.K. Kim, Gas transport in hydrogen electrode of solid oxide regenerative fuel cells for power generation and hydrogen production, Int. J. Hydrogen Energy 39 (2014) 3868-3878, https://doi.org/10.1016/j.ijhydene.2013.12.142.

[3] M. Ball, M. Wietschel, The future of hydrogen - opportunities and challenges, Int. J. Hydrogen Energy 34 (2009) 615-627, https://doi.org/10.1016/j.ijhydene.2008.11.014.

[4] N. Savage, B. Chwieroth, A. Ginwalla, B. R. Patton, S. A. Akbar, P. K. Duttta, Composite n–p semiconducting titanium oxides as gas sensors, Sens. Actuators, B 79 (2001) 17-27, https://doi.org/10.1016/S0925-4005(01)00843-7.

[5] A. Gurlo, M. Sahm, A. Oprea, N. Barsan, U. Weimar, A p- to n-transition on α-Fe_2O_3-based thick film sensors studied by conductance and work function change measurements, Sens. Actuators, B 102 (2004) 291-298, https://doi.org/10.1016/j.snb.2004.04.075.

[6] A. Gurlo, N. Barsan, A. Oprea, M. Sahm, T. Sahm, and U. Weimar, An n- to p-type conductivity transition induced by oxygen adsorption on α-Fe_2O_3, Appl. Phys. Lett. 85 (2004) 2280-2282, https://doi.org/10.1063/1.1794853.

[7] J.X. Wang, X.W. Sun, Y. Yang and C.M.L. Wu, N-P transition sensing behaviors of ZnO nanotubes exposed to NO_2 gas, Nanotechnology, 20 (2009) 465501, https://doi.org/10.1088/0957-4484/20/46/465501.

[8] H. Huang, H. Gong, C. L. Chow, J. Guo, T. J. White, M. S. Tse, and O. K. Tan, Low-temperature growth of SnO_2 nanorod arrays and tunable n–p–n sensing response of a ZnO/SnO_2 heterojunction for

exclusive hydrogen sensors, Adv. Funct. Mater. 21 (2011) 2680-2686, https://doi.org/10.1002/adfm.201002115.
[9] I. Kosc, I. Hotovy, V. Rehacek, R. Griesseler, M. Predanocy, M. Wilke, L. Spiess, Sputtered TiO_2 thin films with NiO additives for hydrogen detection, Appl. Surf. Sci. 269 (2013) 110-115, http://dx.doi.org/10.1016/j.apsusc.2012.09.061.
[10] J. Nowotny, W. Macyk, E. Wachsman, K. Rahman, Effect of Oxygen Activity on the n−p Transition for Pure and Cr-Doped TiO_2, J. Phys. Chem. C 120 (2016) 3221-3228, http://dx.doi.org/10.1021/acs.jpcc.5b12101.
[11] D. E. Williams, Semiconducting oxides as gas-sensitive resistors, Sens. Actuators, B 57 (1999) 1-3, https://doi.org/10.1016/S0925-4005(99)00133-1.
[12] V. Dusastre, D.E. Williams, Selectivity and composition dependence of response of wolframite-based gas sensitive resistors $(MWO_4)x([Sn–Ti]O_2)1−x$ ($0<x<1$; M=Mn, Fe, Co, Ni, Cu, Zn), J. Mater. Chem. 9 (1999) 965-971, https://doi.org/10.1039/jm9960601351.
[13] D. M. Smyth, The role of impurities in insultating transition metal oxides, Prog. Solid St. Chem. 15 (1984) 145-171, https://doi.org/10.1016/0079-6786(84)90001-3.
[14] F. Langer, S. Perl, S. Hofling, M. Kamp, p- to n-type conductivity transition in 1.0 eV GaInNAs solar cells controlled by the V/III ratio, 106 (2015) 063905, https://doi.org/10.1063/1.4909507.
[15] M. Kumar, V.S. Bhati, S. Ranwa, J. Singh, M. kumar, Pd/ZnO nanorods based sensor for highly selective detection of extremely low concentration hydrogen, Sci. Rep. 7 (2017) 236, https://doi.org/10.1038/s41598-017-00362-x.
[16] A.M. Schultz, T.D. Brown, M.P. Buric, S. Lee, K. Gerdes, P. R. Ohodnicki, High temperature fiber-optic evanescent wave hydrogen sensors using La-doped $SrTiO_3$ for SOFC applications, Sens. Actuators, B 221 (2015) 1307-1313, http://dx.doi.org/10.1016/j.snb.2015.07.046.
[17] J. M. Leimert, A. Bartolf, J. Karl, Hydrogen concentration measurement in high temperature applications using hydrogen permeation, Int. J. Hydrogen Energy 41 (2016) 14360-14367, http://dx.doi.org/10.1016/j.ijhydene.2016.05.061.
[18] T. Hübert, L. Boon-Brett, G. Black, U. Banach, Hydrogen sensors – A review, Sens. Actuators, B 157 (2011) 329-352, http://dx.doi.org/10.1016/j.snb.2011.04.070.
[19] A. A. Haidry, A. E. Stahl, B. Saruhan, Effect of Pt/TiO_2 interface on room temperature hydrogen sensing performance of memristor type $Pt/TiO_2/Pt$ structure, Sens. Actuators, B 253 (2017) 1043-1054, http://dx.doi.org/10.1016/j.snb.2017.06.159.
[20] T. Plecenik, M. Mosko, A.A. Haidry, P. Durina, M. Truchly, B. Grancic, M. Gregor, T. Roch, L. Satrapinskyy, A. Moskova, M. Mikula, P. Kus, A. Plecenik, Fast highly-sensitive room-temperature semiconductor gas sensor based on the nanoscale $Pt–TiO_2–Pt$ sandwich, Sens. Actuators, B 207 (2015) 351-361, http://dx.doi.org/10.1016/j.snb.2014.10.003.
[21] A.A. Haidry, Cagdas Cetin, Klemens Kelm, Bilge Saruhan, Sensing mechanism of low temperature NO_2 sensing with top–bottom electrode (TBE) geometry, Sens. Actuators, B 236 (2016) 874-884, http://dx.doi.org/10.1016/j.snb.2016.03.016.
[22] L. Sun, A. A. Haidry, Q. Fatima, Z. L, and Z. Yao, Improving the humidity sensing below 30% RH of TiO_2 with GO Modification, Mater. Res. Bull. 99 (2018) 124-131, http://dx.doi.org/10.1016/j.materresbull.2017.11.001.
[23] Z. Li, A. A. Haidry, T. Wang, Z. J. Yao, Low-cost fabrication of highly sensitive room temperature hydrogen sensor based on ordered mesoporous Co-doped TiO_2 structure, Appl. Phys. Lett. 111 (2017) 032104, https://doi.org/10.1063/1.4994155.
[24] Z. Li, A. A. Haidry, B. Gao, T. Wang, Z. J. Yao, The effect of Co-doping on the humidity sensing properties of ordered mesoporous TiO_2, Appl. Surf. Sci. 412 (2017) 638-647, https://doi.org/10.1016/j.apsusc.2017.03.156.

[25] T. Roch, E. Dobrocka, M. Mikula, A. Pidık, P. Durina, A.A. Haidry, T. Plecenik, M. Truchly, B. Grancic, A. Plecenik, P. Kus, Strong biaxial texture and polymorph nature in TiO_2 thin film formed by ex-situ annealing on c-plane Al_2O_3 surface, J. Cryst. Growth 338 (2012) 118-124, http://dx.doi.org/10.1016/j.jcrysgro.2011.10.053.
[26] T. Luttrell, S. Halpegamage, J. Tao, A. Kramer, E. Sutter, M. Batzill, Why is anatase a better photocatalyst than rutile? - Model studies on epitaxial TiO_2 films, Scientific Reports 4 (2014) 4043, http://dx.doi.org/10.1038/srep04043.
[27] A. A. Mosquera, J. M. Albella, V. Navarro, D. Bhattacharyya, J. L. Endrino, Effect of silver on the phase transition and wettability of titanium oxide films, Scientific Reports 6 (2016) 32171, http://dx.doi.org-/10.1038/srep32171.
[28] U. Diebold, The surface science of titanium dioxide, Surf. Sci. Rep. 48 (2003) 53-229, https://doi.org/10.1016/S0167-5729(02)00100-0.
[29] A.Z. Sadek, J. G. Partridge, D. G. McCulloch, Y. X. Li, X. F. Yu, W. Wlodarski, K. Kalantar-zadeh, Nanoporous TiO_2 thin film based conductometric H_2 sensor, Thin Solid Films, 518 (2009) 1294-1298, http://dx.doi.org/10.1016/j.tsf.2009.02.151.
[30] Weerasak Chomkitichai, Hathaithip Ninsonthi, Chaikarn Liewhiran, Anurat Wisitsoraat, Saengrawee Sriwichai, Sukon Phanichphant, Flame-Made Pt-Loaded TiO_2 Thin Films and Their Application as H_2 Gas Sensors, Journal of Nanomaterials, 2013 (2013) 497318, http://dx.doi.org/10.1155/2013/497318.
[31] J. Moon, H. Hedman, M. Kemell, A. Tuominen, R. Punkkinen, Hydrogen sensor of Pd-decorated tubular TiO_2 layer prepared by anodization with patterned electrodes on SiO_2/Si substrate, Sens. Actuators, B 222 (2016) 190-197, http://dx.doi.org/10.1016/j.snb.2015.08.054.
[32] S.K. Hazra, S. Basu, High sensitivity and fast response hydrogen sensors based on electrochemically etched porous titania thin films, Sens. Actuators, B 115 (2006) 403-411, http://dx.doi.org/10.1016/j.snb.2005.10.002.
[33] B. Lyson-Sypien, A. Czapla, M. Lubecka, E. Kusior, K. Zakrzewska, M. Radecka, A. Kusior, A.G. Balogh, S. Lauterbach, H.-J. Kleebe, Gas sensing properties of TiO_2–SnO_2 nanomaterials, Sens. Actuators, B 187 (2013) 445-454, http://dx.doi.org/10.1016/j.snb.2013.01.047.
[34] D. Ponnusamy, A. K. Prasad, S. Madanagurusamy, CdO-TiO_2 nanocomposite thin films for resistive hydrogen sensing, Microchim Acta 183 (2016) 311-317, http://dx.doi.org/10.1007/s00604-015-1653-y.
[35] N. Yamazoe, K. Shimanoe, Theory of power laws for semiconductor gas sensors, Sens. Actuators, B 128 (2008) 566-573, https://doi.org/10.1016/j.snb.2007.07.036.
[36] W-T. Koo, S. Qiao, A. F. Ogata, G. Jha, J-S. Jang, V. T. Chen, ID. Kim, R. M. Penner, Accelerating Palladium Nanowire H_2 Sensors Using Engineered Nanofiltration, ACS Nano, 11 (2017) 9276-9285, http://dx.doi.org/10.1021/acsnano.7b04529.
[37] A.A. Haidry, N. Kind, B. Saruhan, Investigating the influence of Al-doping and background humidity on NO_2 sensing characteristics of magnetron-sputtered SnO_2 sensors, J. Sens. Sens. Syst. 4 (2015) 271-280, http://dx.doi.org/10.5194/jsss-4-271-2015.
[38] A.A. Vasiliev, M.A. Polykarpov, Change of ferric oxide (Fe_2O_3) semiconductor conductivity type in the interaction with reducing gases, Sens. Actuators, B 7 (1992) 626-629, https://doi.org/10.1016/0925-4005(92)80376-9.
[39] B.W. Licznerski, K. Nitsch, H. Teterycz, K. Wisniewski, The influence of Rh surface doping on anomalous properties of thick-film SnO_2 gas sensors Sens. Actuators, B 79 (2001) 157-162, http://dx.doi.or-g/10.1016/S0925-4005(01)00862-0.
[40] K. Galatsis, L. Cukrov, W. Wlodarski, P. McCormick, K. Kalantar-Zadeh, E. Comini, G. Sberveglieri, P- and n-type Fe-doped SnO_2 gas sensors fabricated by the mechanochemical processing technique Sens. Actuators B 93 (2003) 562-565, http://dx.doi.org/10.1016/S0925-4005(03)00233-8.

[41] B. Lyson-Sypien, A. Czapla, M. Lubecka, P. Gwizdz, K. Schneider, K. Zakrzewska, K. Michalow, T. Graule, A. Reszka, M. Rekas, A. Lacz and M. Radecka, Nanopowders of chromium doped TiO_2 for gas sensors Sens. Actuators, B 175 (2012) 163-172, http://dx.doi.org/ 10.1016/j.snb.2012.02.051.

[42] M.T. McDowell, M.F. Lichterman, A.I. Carim, R. Liu, S. Hu, B.S. Brunschwig, N.S. Lewis, The Influence of Structure and Processing on the Behavior of TiO_2 Protective Layers for Stabilization of n-Si/TiO_2/Ni Photoanodes for Water Oxidation ACS Appl. Mater. Interfaces 7 (2015) 15189-15199, http://dx.doi.org/ 10.1021/acsami.5b00379.

[43] A. A. Haidry, P. Schlosser, P. Ďurina, M. Mikula, M. Tomášek, T. Plecenik, T. Roch, A. Pidík, M. Štefečka, J. Noskovič, M. Zahoran, P. Kúš, A. Plecenik, Hydrogen gas sensors based on nanocrystalline TiO_2 thin films, Cent. Eur. J. Phys. 9 (2011) 1351-1356, http://dx.doi.org/10.2478/s11534-011-0042-3.

[44] F. Bensouici, T. Souier, A. A. Dakhel, A. Iratni, R. Tala-Ighil and M. Bououdina, Synthesis, characterization and photocatalytic behavior of Ag doped TiO_2 thin film, Superlattices and Microstructures, 85 (2015) 255-265, http://dx.doi.org/10.1016/j.spmi.2015.05.028.

[45] H. Chaker, L. Chérif-Aouali, S. Khaoulani, A. Bengueddach, S. Fourmentin, Photocatalytic degradation of methyl orange and real wastewater by silver doped mesoporous TiO_2 catalysts， Journal of Photochemistry and Photobiology A: Chemistry 318 (2016) 142-149, http://dx.doi.org/10.1016/j.jphotochem.2015.11.025.

[46] M. W. den Otter, Approximate expressions for the capacitance and electrostatic potential of interdigitated electrodes, Sens. Actuators, A 96 (2002) 140-144, http://dx.doi.org/10.1016/S09244247(01)00783-X.

[47] R. Konenkamp, Carrier transport in nanoporous TiO_2 films, Phys. Rev. B 61 (2000) 11057, http://dx.doi.org/10.1103/PhysRevB.61.11057.

Figure(s)

Table 1: Comparison of the current work highlights with previous works.

Sensor system	Background condition	C_{H2} (ppm)	T (°C)	Sensor Response	Voltage(V)	Remarks
Nanoporous TiO_2	Dry air	1250	225	1.13	-	Nanoporous TiO_2 was prepared by anodization [29].
	Humid air	Not Reported (NR)				
TiO_2	Dry air	150	300-400	-	-	Flame-spray-made unloaded TiO_2; selectivity was not reported [30].
	Humid air	Not Reported (NR)				
Pt-TiO_2	Dry air	40	300-400	1.1	-	Flame-spray-made Pt-loaded TiO_2 nanopowders [30].
	Humid air	Not Reported (NR)				
Pd-TiO_2	Dry air	10	180	1.25	5V	Anodization of Ti film obtained Pd-decorated TiO_2 tubular structures, which showed good selectivity to CO, CO_2, ethanol and acetone [31].
	Humid air	1-50	140-180	-		
	N_2	10	180	25		
Al-TiO_2	Dry air	500	200-400	1.3	-	Aluminium doped porous titania (TiO_2) thin films were grown by thermal oxidation. [32]
	Humid air	Not Reported (NR)				
NiO-TiO_2	Dry air	300	200	1.47	-	P-type to n-type transition was mentioned [9].
	Humid air	Not Reported (NR)				
SnO_2-TiO_2	Dry air	50	300	0.9	-	$S=(R_0-R)/R_0$ [33]
	Humid air	Not Reported (NR)				
CdO-TiO_2	Dry air	500	275	0.3-3.06%	0.25V	$\%S = (R_0-R)/R_0 \times 100$ [34]
	Humid air	Not Reported (NR)				

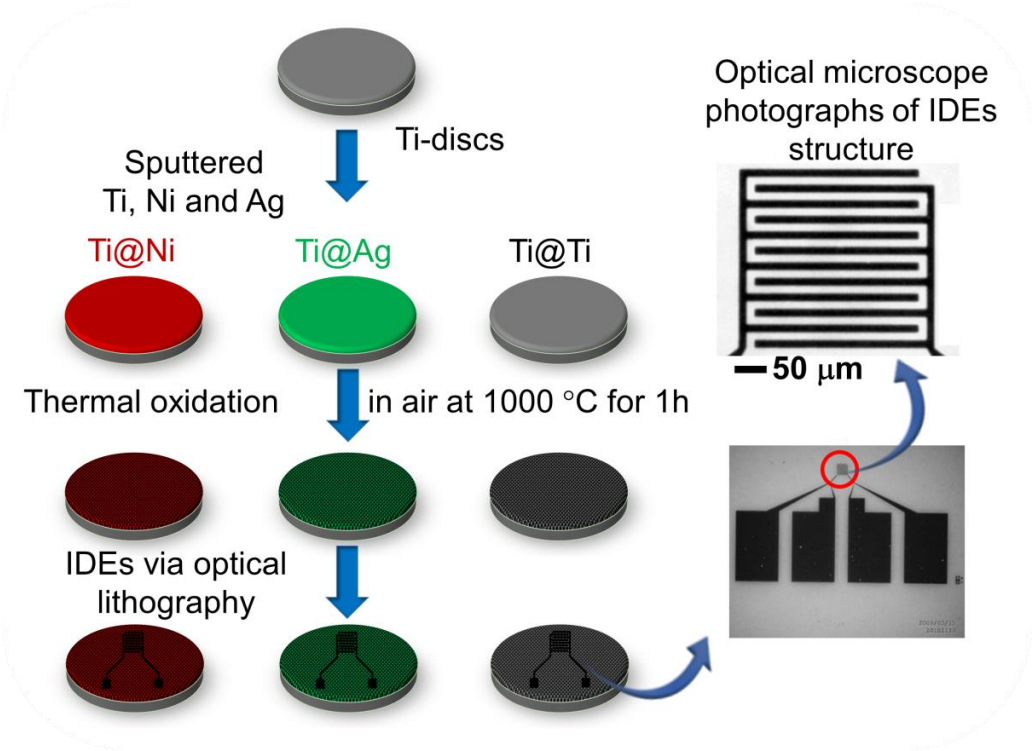

Fig. 1 (color online) The schematic diagram showing the fabrication process of gas sensors based on TiO_2 films with TiO_2, NiO and Ag_2O modification, the figure also includes the optical microscope photographs of interdigitated electrodes (IDEs) structure, the scale bar on the most top right optical microscope photograph of the comb-like Pt electrodes with 10 μm spacing indicates the scale of 50 μm.

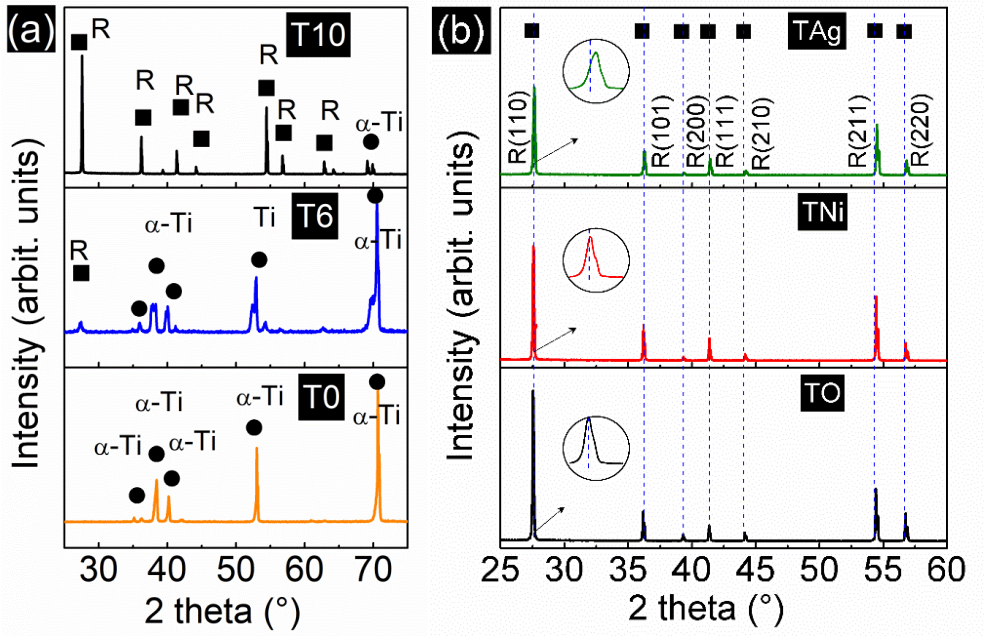

Fig. 2 (color online) The XRD diffractograms of as-received Ti-discs (T0) and oxidized Ti-discs at 600 °C (T6) and 1000°C (T10) are shown in (a). The comparative diffractograms of Ti-discs modified with Ti (TO), Ni (TNi), and Ag (TAg), the inset of each curve shows variation in peak intensity and right shift of the zoomed R (110) crystal in (b). The XRD diffractograms were

compared with standard powder diffraction card JCPD-44-1294 (α-Ti with hexagonal closed packed, a = 2.9504 Å, c = 4.6833 Å and c/a ratio of ~1.587) and JCPDS-21-1276 (rutile with tetragonal symmetry of space group $P4_2/mnm$ with *a* = b = 4.5933 Å, *c* = 2.9592 Å and c/a ratio of ~0.644).

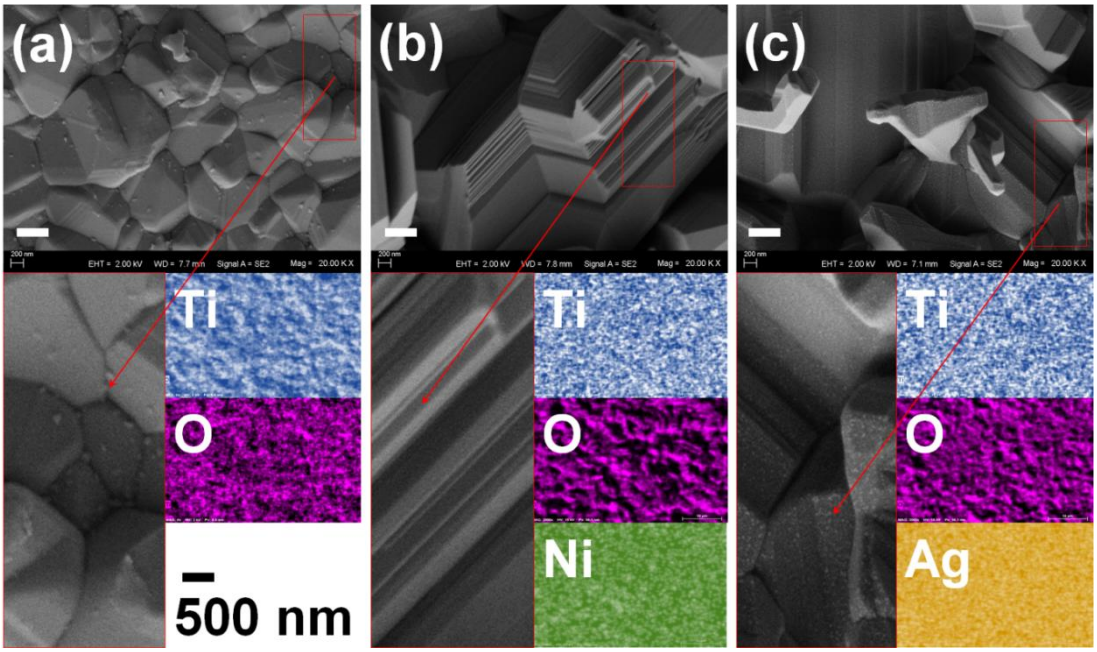

Fig. 3 (color online) The SEM and EDS analysis of TiO_2@TiO_2 (a), TiO_2@NiO (b), and TiO_2@AgO (c) oxidized discs. The enlarged SEM micrographs and EDX elemental mapping of these samples are shown on bottom figure. Solid white lines in a-c indicate the 500 nm scale bar in SEM micrographs. The EDX analysis of TiO_2@NiO (b) and TiO_2@AgO (c) confirms the presence of NiO and AgO due to thermal oxidation process.

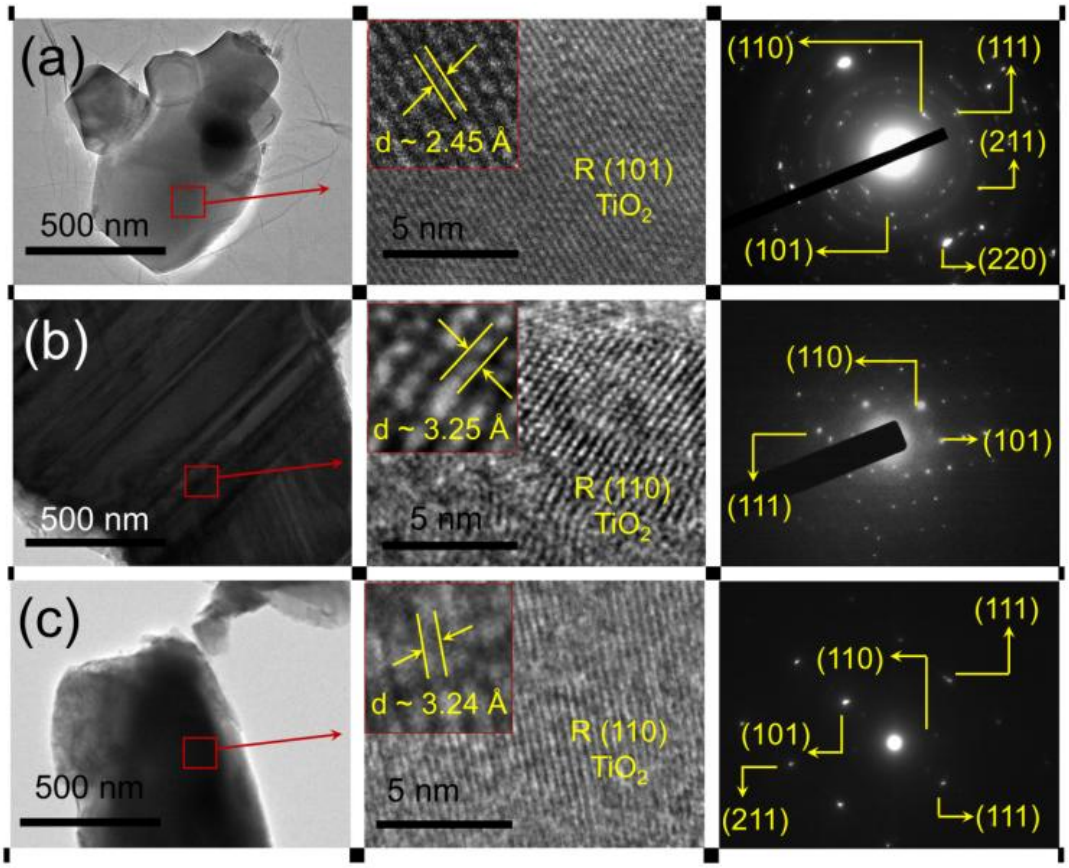

Fig. 4 (color online) The TEM micrographs of TiO_2@TiO_2 (a), TiO_2@NiO (b), and TiO_2@AgO (c) oxidized discs are shown on left figures. The middle figures show corresponding HRTEM images with the inset shows magnified HR image and estimated d-spacing values for each samples. The figures on the right show respective selected area diffraction (SAED) pattern.

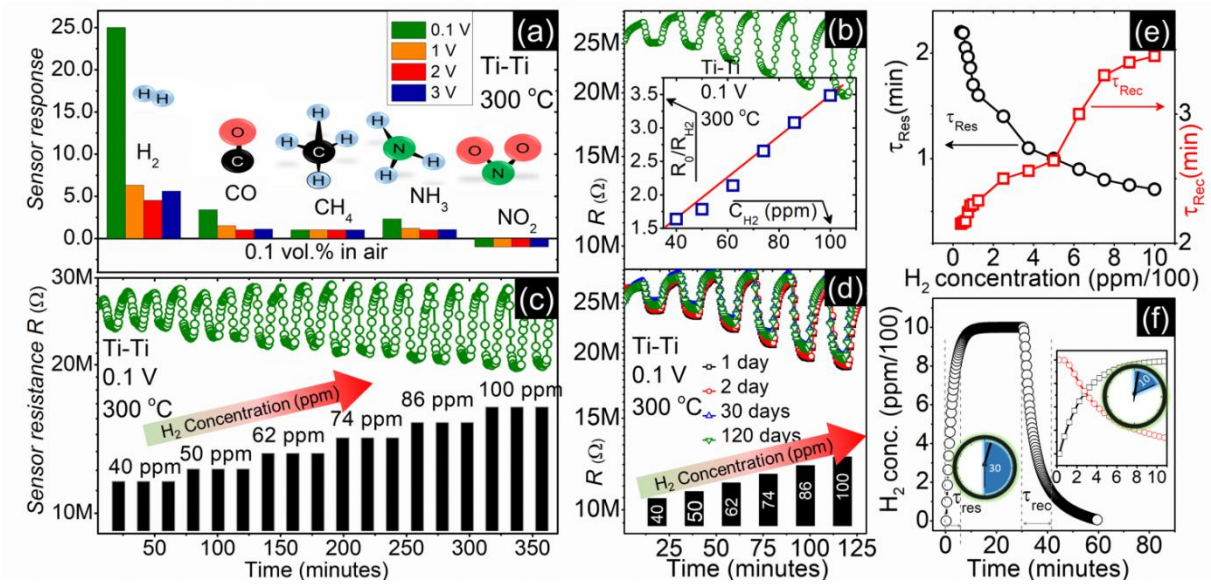

Fig. 5 (Color online) Selectivity of the sensors to hydrogen against other gases such as CO, CH_4, NH_3, and NO_2 is shown in (a). Hydrogen gas sensing characteristics of TiO_2@TiO_2 sensors, the typical real time changes in the electrical resistance upon the gas in/out cycles, id est

dynamic-responses, to sequential cycles of 40, 50, 62, 74, 86 and 100 ppm hydrogen gas balanced in technical air (a). The dynamic responses were recorded by using in-house made software in LabVIEW with a fixed time (10 minutes) for each sequential cycle at operating at 300 °C with 0.1V biasing. Inset: The plots of sensor response ($S = R_0 / R_g$) versus increasing hydrogen gas concentrations for the TiO_2@TiO_2 sensors evaluated from the dynamic responses of the sensors presented in (b). The sensor responses were calculated from the ratio of stable base resistance in air (R_0) to saturated resistance value (R_g) in specific hydrogen concentration (62 – 1000 ppm). The long term and short term stability of the sensors is demonstrated in (c) and (d) respectively. The x-axis scales on (b) and (d) are same. The estimated response (τ_{Res}) and recovery (τ_{Rec}) times plotted against hydrogen concentration (62 – 1000 ppm) are shown in (e). The simulated plot of typical H_2 1000 ppm concentration evolution of 30 minutes cycle inside the chamber is shown in (f). Inset: The zoom-in (enlarge) view of the simulated plot of 1000 ppm H_2 evolution inside the chamber for initial 10 minutes, the y-axis scale is equal to the scale of main plot.

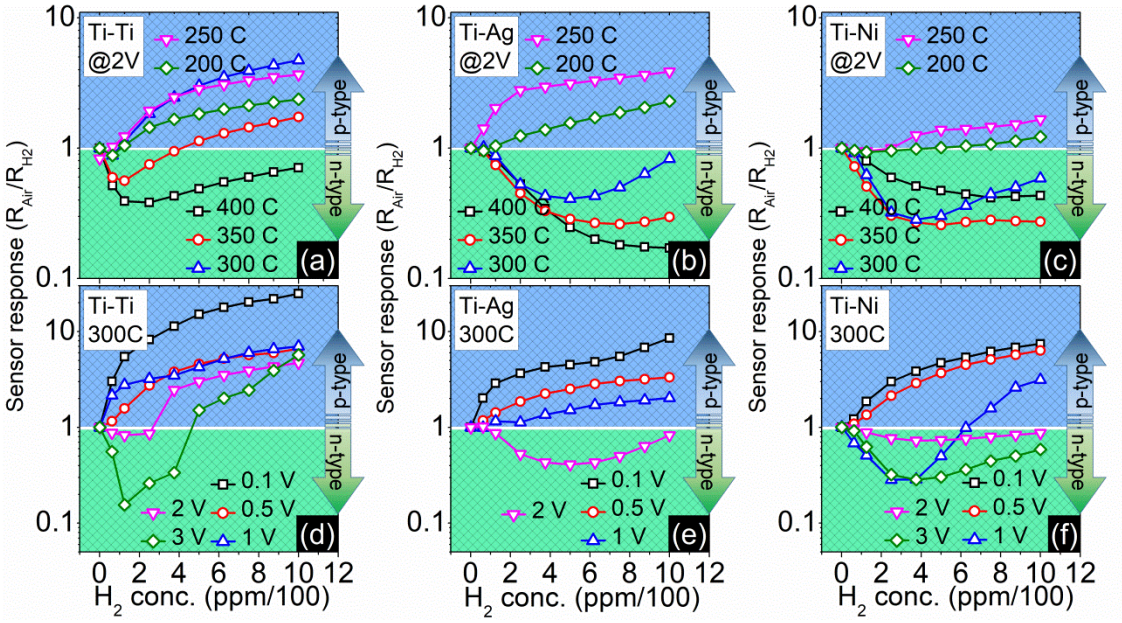

Fig. 6 (color online) The plots of sensor response ($S_R = R_0 / R_g$) as a function of hydrogen gas concentrations (C_{H2}) at various working temperatures 200 °C (green open diamond ◇), 250 °C (magenta open down-triangle ▽), 300 °C (blue open up-triangle △), 350 °C (red open circle ○) and 400 °C (black open squares □) for the sensors based on Ti-Ti (a), Ti-Ag (b) and Ti-Ni (c), the S_R values were evaluated from step-like transient responses recorded at 2 V. The plots of sensor response S_R as a function of hydrogen gas concentrations (C_{H2}) at various working temperature 300 °C for the sensors based on Ti-Ti (a), Ti-Ag (b) and Ti-Ni (c), the S_R values were evaluated from step-like transient responses recorded at various voltages 0.1 V (black open squares □), 0.5 V (red open circle ○), 1 V (blue open up-triangle △), 2 V C (magenta open down-triangle ▽) and 3 V (green open diamond ◇).

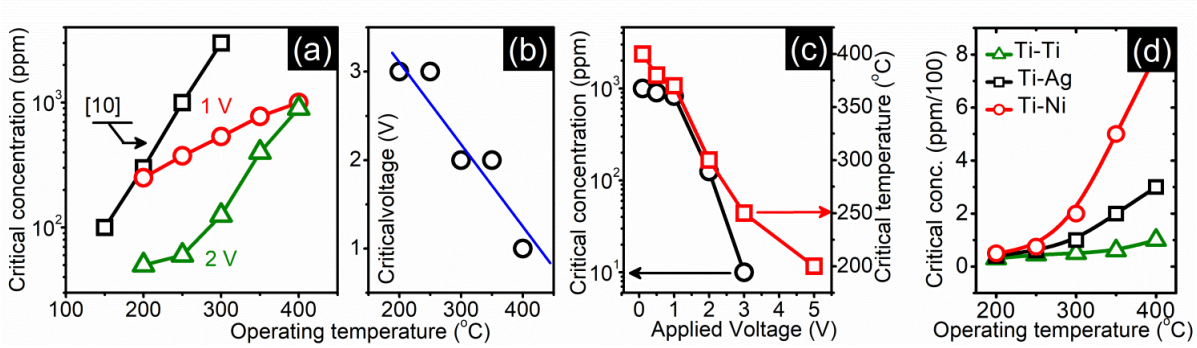

Fig. 7 (color online) The interdependence of critical concentration, critical temperature and critical voltage. The plot of critical concentration and critical applied voltage against working temperature is shown in (a) and (b). The values of critical concentration and applied voltage are taken from step-like measurements of TiO_2-TiO_2 samples measured at 1 V (red open circle ○) and 2 V (green open up-triangle △), the data plotted as black open box □ were measured at 1 V by I. Kostic et al. [10].

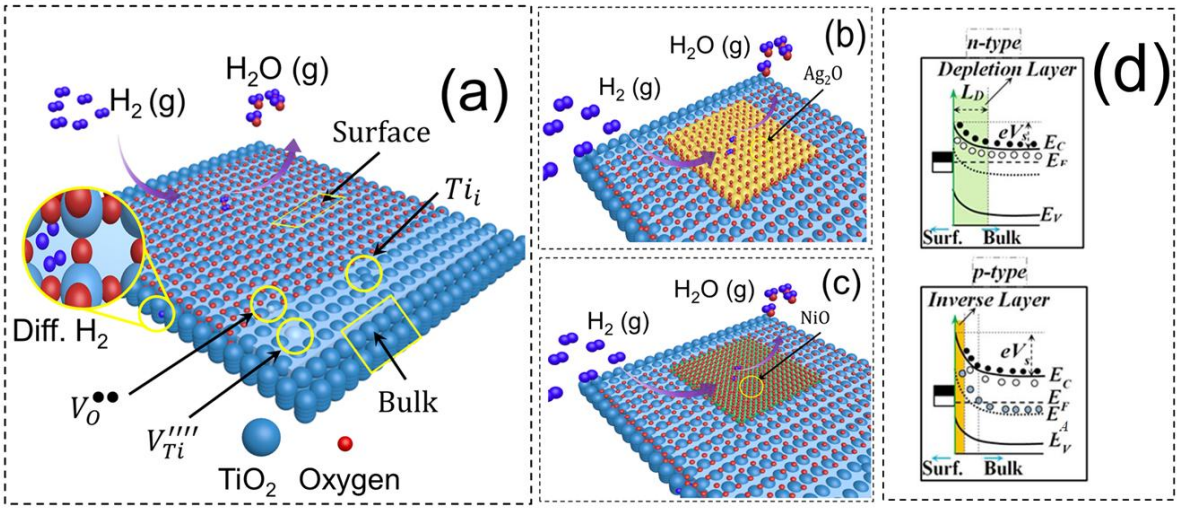

Fig. 8 (color online) The illustration of sensing mechanism with physical-chemical method, H_2 surface reaction, H_2 diffusion through the surface, various kinds of defects related to O, Ti vacancies, Ti interstitials and the representation of bulk TiO_2 and oxygen rich surface (a). The reaction of H_2 gas with Ag_2O (b) and NiO (c) modified TiO_2-surface. The band bending schematic representation of n- and p-type TiO_2 responses is shown in (d). For n-type the conductivity is dominated by the depletion layer where the Fermi level lies near the conduction level and the majority carriers are electrons (on left). On the other hand, for p-type surface the inverse layer is formed where the Fermi level is situated near the donor energy level and the majority carriers are holes (on right). Here electrons, oxygen vacancies and holes are represented by filled black circles ●, open circles ○, and striped circles ⊕, respectively. The energy bands E_C, E_F, E_D and E_V represent conduction, Fermi, donor and valence energy level respectively, L_D is the Debye length of the depletion layer and qV_S is the height of surface potential barrier. The figure also depicts the mechanism behind conductivity inversion with threshold concentration (C_{Th}), threshold temperature (T_{Th}) and critical applied voltage along with TiO_2 surface modification with Ag_2O or

NiO forming a heterojunction.

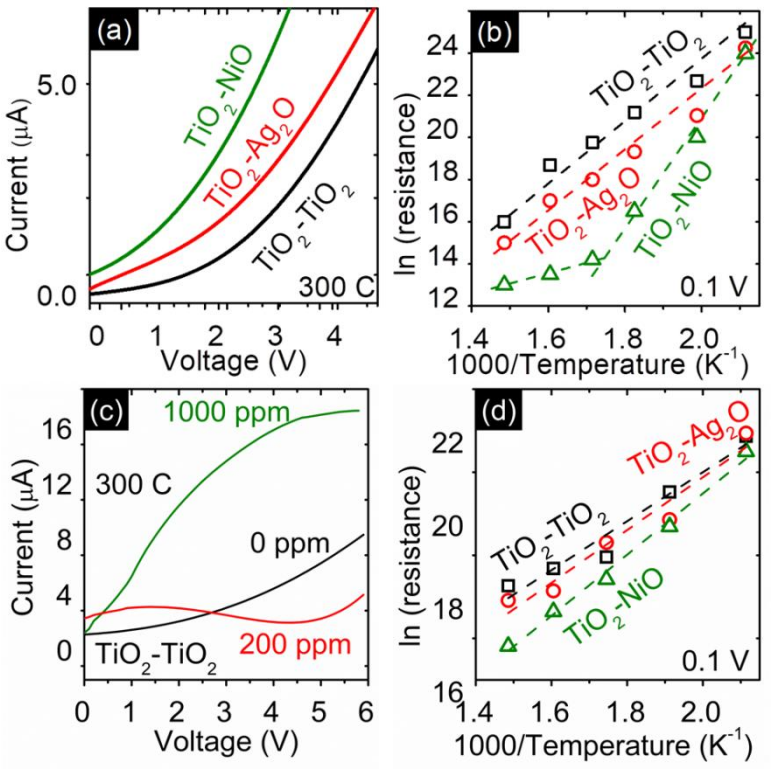

Fig. 9 (color online) The current-voltage (I-V) characteristics performed in dry air flow at 300° C (a). The extracted Arrhenius plots for TiO_2-TiO_2, TiO_2-Ag_2O and NiO samples from operating temperature (200 – 400 °C) dependent resistance measurement in dry air flow (b). Here, the symbols indicate the original data points and dashed-lines indicate the linear fit. The current-voltage (I-V) characteristics performed for TiO_2-TiO_2 sample in 0, 200 and 1000 ppm H_2 flow at 300° C (c). The extracted Arrhenius plots for TiO_2-TiO_2, TiO_2-Ag_2O and NiO samples from operating temperature (200 – 400 °C) dependent resistance measurement 200 H_2 flow (d).

Supplementary Material

Click here to download Supplementary Material: SNB-03-2018-NUAA-DLR-UNIBA_ESI.docx

Author Biographies

Azhar Ali Haidry received his Bachelor and Master Degrees in Pakistan at the Bahauddin Zakariya University (BZU) in Multan. From 2004 to 2008, he taught Physics at BZU and Virtual University (VU) of Pakistan. He carried out his PhD-study from September 2009 to May 2013 under the supervision of Prof. Dr. Andrej Plecenik at Comenius University Bratislava in Slovakia on “micro- to nano-scaled metal oxide gas sensors”. From 08.2013 to 03.2016, he has worked as a Post-Doc at the Institute of Materials Research of the German Aerospace Center (DLR) on semiconductor based gas sensors. Currently, Dr. Haidry is working as Associate Professor at College of Materials Science and Technology, Nanjing University of Aeronautics and Astronautics (NUAA). His research interests are in the field of nanotechnology, functional coatings, material characterization, metal oxide, chemical sensors and scanning electron microscopy.

Linchao Sun received his Bachelor Degree at Nanjing University of Aeronautics and Astronautics in China. Now he is a master student, working at College of Materials Science and Technology (MST), Nanjing University of Aeronautics and Astronautics (NUAA). His research area is focused on gas sensors based on metal oxide semiconductor.

Bilge Saruhan is a materials scientist with PhD degree on advanced ceramic materials from the University of Limerick/Ireland and lecturing qualification (Habilitation) on nanostructured functional materials and composites from the Technical University of Freiberg/Germany. She received her BSc from the Dept. of Materials and Metallurgical Engineering of Istanbul Technical University (ITU) and her MSc in Materials Science from the Faculty of Chemistry and Metallurgy of ITU. Since completion her PhD, she has been working at the Institute of Materials Research of the German Aerospace Center (DLR) in Cologne/Germany where she presently leads the activities on functional coatings with emphasis on sensors and battery-like supercapacitor electrodes. Her research interests cover ceramic matrix composites, thermal barrier coatings, gas sensors, catalytic materials and energy

storage materials. Up to date, she has authored/co-authored 112 papers, published 1 book and holds 7 (3 pending) patents.

Andrej Plecenik is professor of physics at the Faculty of Mathematics, Physics andInformatics of the Comenius University in Bratislava. He is employed at the Depart-ment of Experimental Physics, Faculty of Mathematics, Physics and Informatics,Comenius University in Bratislava since 2002. His research interests are focusedon nanotechnology, metal oxide gas sensors and superconductivity.

Honglie Shen is a professor of Nanjing University of Aeronautics and Astronautics in China. He focuses on advanced photoelectric / electro-optical conversion materials and devices, new functional thin film and sensing technology, new energy materials and application technology and solar cell key materials and technology research.

Zhengjun Yao received his Bachelor and Master Degrees at Southeast University and Xi'an Jiaotong University in China, respectively. He received his Ph.D. degree from the Institute of Mechanical Engineering and Automation of Nanjing University of Aeronautics and Astronautics in China in 2004. Now he is a professor of College of Materials Science and Technology at Nanjing University of Aeronautics and Astronautics in China.